

Electrical Catalysis of Forbidden Transitions in Single-Molecule Devices

Ruihao Li, Ran Liu, Shima Ghasemi, Pedro Ferreira, Dianting Zou, Feng Sun, Kasper Moth-Poulsen,* and Joshua Hihath*

Molecular orbital symmetry plays a pivotal role in determining chemical reaction mechanisms. The process of changing chemical reactants into products must transition along a pathway that conserves molecular orbital symmetry to ensure continuity. This principle is so fundamental that reactions that do not conserve symmetry are typically considered “forbidden” due to the high resultant energy barriers. Here, it is demonstrated that it is possible to electrically catalyze these forbidden transitions when a single molecule is bound between two electrodes in a nanoscale junction. A cycloaddition reaction is induced in a norbornadiene (NBD) derivative, converting it to quadricyclane (QC) by utilizing nanoconfinement to place the molecule into a configuration that is far from equilibrium and applying a small voltage to the molecular junction. Traditionally, this reaction can only be induced photochemically due to orbital symmetry selection rules. By directly tracking the reaction dynamics *in situ* using single-molecule Raman spectroscopy, it is shown that for this reaction to be electrically catalyzed the molecule must be sterically maneuvered into a configuration near the transition state at the peak of the energy barrier prior to applying the voltage needed to successfully induce the forbidden transition is applied.

1. Introduction

The next generation of adaptive and energy-related materials requires molecular building blocks that can be switched rapidly, reversibly and with minimal energy input, but most structurally

rich isomers remain locked within steep energy barriers that limit their functionalization. Nature solves this problem with enzyme active sites, which utilize a combination of molecular confinement, built-in electric fields, reactant proximity, and transition state stabilization to lower activation energies to allow reactions to proceed at much higher rates than can be achieved otherwise.^[1–3] Because of the high turnover rates, and selectivity of these systems, there has been growing interest in the development of so-called “artificial enzymes” that utilize these principles to significantly enhance specific reactions,^[4] and recently, single-molecule electrical junctions have emerged as a new pathway for inducing and controlling chemical reactions.^[5,6] However, in these systems it is often difficult to determine the role of nanoconfinement in controlling these reactions. In this work, we utilize a single-molecule break junction (SMBJ) system, combined with single-molecule Raman spectroscopy to create a type of

artificial enzyme that can not only induce nanoconfinement and modify the built-in applied voltage, but can also directly track the reaction process and provide insights into the role of nanoconfinement and state stabilization on the reaction mechanism. As an initial reaction, we focus on a [2+2] cycloaddition reaction that

R. Li, R. Liu, D. Zou, J. Hihath
 Biodesign Center for Bioelectronics and Biosensors at Arizona State University
 Tempe, AZ 85287, USA
 E-mail: jhihath@asu.edu

S. Ghasemi, K. Moth-Poulsen
 Department of Chemistry and Chemical Engineering
 Chalmers University of Technology
 Gothenburg 41296, Sweden
 E-mail: kasper.moth-poulsen@upc.edu

P. Ferreira, K. Moth-Poulsen
 Department of Chemical Engineering
 Universitat Politècnica de Catalunya
 EEBE, Eduard Maristany 10-14, Barcelona 08019, Spain

F. Ferreira, K. Moth-Poulsen
 The Institute of Materials Science of Barcelona
 ICMAB-CSIC, Bellaterra, Barcelona 08193, Spain
 F. Sun
 School of Physics
 Ningxia University
 Yinchuan 750021, P. R. China
 K. Moth-Poulsen
 Catalan Institution for Research & Advanced Studies, ICREA
 Pg. Lluís Companys 23, Barcelona 08010, Spain
 J. Hihath
 School of Electrical, Computer, and Energy Engineering
 Arizona State University
 Tempe, AZ 85287, USA

 The ORCID identification number(s) for the author(s) of this article can be found under <https://doi.org/10.1002/adma.202511822>

DOI: 10.1002/adma.202511822

is typically forbidden by orbital symmetry selection rules, and has yet to be demonstrated in conventional enzymatic systems.^[7]

Orbital symmetry selection rules were developed by Woodward and Hoffmann in the mid-20th century, and enabled a detailed understanding of pericyclic reaction mechanisms, which in turn provided insights into a range of complex chemical reactions.^[8] At its heart, this theory dictates that the symmetry of the molecular orbitals in the reactants must match the symmetry of the transition states and the products. This model is so fundamental that Woodward and Hoffmann once stated that it would take a very powerful Maxwell demon to bypass these selection rules.^[9] Recently, mechanical forces have been used to bypass these selection rules in certain instances,^[10,11] however, achieving precise control over such reactions at the molecular level and understanding their dynamic pathways remains a formidable challenge. To address this limitation, we investigate these transitions at the single-molecule scale, where precise steric control and observation can provide insights into the dynamics of forbidden chemical transformations. We combine single-molecule break junction methods, which have emerged as powerful tools for constructing single-molecule devices, probing their electrical transport properties, and inducing reactions^[6,12] with single-molecule Raman spectroscopy to reveal vibrational fingerprints with spatial and chemical specificity. The integration of these two techniques presents a promising approach to simultaneously capture electronic and vibrational signatures of molecular processes at the single-molecule level.

Here, we demonstrate this biomimetic catalysis strategy that utilizes a combination of nanoconfinement^[1,13] and electrostatic catalysis^[5,14,15] can act as such Maxwell demon, and allow standard molecular orbital conservation rules to be overcome. We specifically focus on electrically catalyzing a Norbornadiene (NBD) derivative into its Quadricyclane (QC) form by applying a modest voltage bias across a single-molecule junction.^[16–18] The standard, photochemically induced cycloaddition reaction from NBD to QC is the quintessential example of orbital symmetry conservation.^[7,19,20] As shown in **Figure 1a**, the Highest Occupied Molecular Orbital (HOMO) of the NBD and QC forms have different symmetries. For the NBD form, the phase of the wavefunctions on carbon atoms C3 and C4 have opposite phases (blue molecular conformation, **Figure 1a**), as such, creating a bonding state between these two atoms as in the QC form (red conformation) requires significant bond rotation.^[21] Because of this asymmetry, there is a large energy barrier ($E_B \approx 2.7$ eV (62.3 kcal mol⁻¹)) preventing direct conversion from NBD to QC (dotted gray line, **Figure 1a**).^[22] However, C3 and C4 have the same phase orientation for the LUMO level of NBD (denoted NBD* in **Figure 1a**), and thus only a small rotation is required to form a bonding state. Thus, this reaction is normally induced by placing NBD in an excited state photochemically, once in this state, there is a natural tendency for the system to relax into the QC form through disrotatory rotation of the carbon atoms on the ends of the π -bonds (solid gray line, **Figure 1a**).^[7] We employ single-molecule Raman spectroscopy^[23–27] on a single-molecule break junction^[28–31] system to allow direct interrogation of the molecular configuration while tracking the electrically-controlled switching behavior. This combined system enables simultaneous electrical and mechanical control, electrical characterization, and chemical mapping at the single-molecule level (**Figure 1b**).^[32]

This allows mechanical control over the molecular configuration while the Raman spectra provide a fingerprint of the molecular bonds,^[33–35] thus allowing the states to be directly observed and manipulated to provide insights into the dynamics of chemical transformations and examination of the reaction processes (**Figure 1c**).^[6,36,37]

To begin, we first demonstrate that the reaction between the NBD and QC can be electrically induced in a single-molecule junction.^[38] Single-molecule electrical catalysis has recently emerged as a unique mechanism for inducing chemical reactions at the nanoscale.^[5,14,15] In this case, we utilize an NBD-derivative with oligo-phenylene-ethynylene (OPE) side chains that are terminated with thioacetate end groups capable of binding to the gold electrodes (see Experimental Section).^[38,39] To measure the switching behavior, we first separate the electrodes by a small-gap on the order of ≈ 1.0 nm, and then use a feedback system to stabilize the gap separation. In this configuration, we focus the Raman laser on the nanocavity between the two electrodes by finding the maximum intensity of the Raleigh scattering from the junction. At this point we turn off the feedback and allow molecules to intermittently bind between the two electrodes. When a molecule binds to the two electrodes, there is a sudden increase in the electrical conductance measured between the two electrodes which can last from a few milliseconds to several seconds. During these so-called “blinking events”, we can observe changes in the junction conductance that are consistent with the conductance of the molecule,^[40] and notably these blinking-events are correlated with sudden changes in the intensity of the Raman signal (see **Figure S4**, Supporting Information).^[41,42] These correlated signals confirm the single-molecule nature of both the molecular junction and the Raman signal.^[43] As shown in **Figure S2** (Supporting Information), at 0.05 V, the conductance is $10^{-4.0}$ G₀ (≈ 7.75 nS, note G₀ is the conductance quantum ≈ 77.48 μ S), which is consistent with the NBD-form, and at 0.55 V, the conductance is $10^{-4.7}$ G₀ (≈ 1.54 nS), which is ascribed to the QC-form.^[38] We note that at higher biases the conductance of the junction is lower, thus providing a clear indicator of the switching behavior.

To drive the reaction between the NBD-form and the QC-form *in situ* we apply a square-wave voltage to the junction that switches between 0.05 and 0.55 V once a conductance blinking event is observed. As can be seen in **Figure 2a**, as the bias is switched between these two values, the conductance reversibly switches between the “high” and “low” states, and the corresponding Raman spectra show a range of peaks between 150 and 600 cm⁻¹. Of particular note is the clear changes in the peak at ≈ 400 cm⁻¹. This low energy mode corresponds to a collective twisting mode within the core unit of the molecule (see **Figure 2d**), in the NBD form, where the vibration is dominated by the out-of-plane twist of C1 and C4. However, after transformation into QC and with the increase in core rigidity, this mode is red shifted and dominated by C5 and C6 movement, with decreased amplitude on C1 and C4. To analyze the Raman spectra in detail and understand any changes in the spectral features when the molecule switches between the NBD and QC forms, we separate each bias domain and calculate the average Raman spectra for each region. The lower panel of **Figure 2b** shows the averaged spectra for each time region labeled from A to H. From these spectra we can see a reversible change in the 400 cm⁻¹ peak

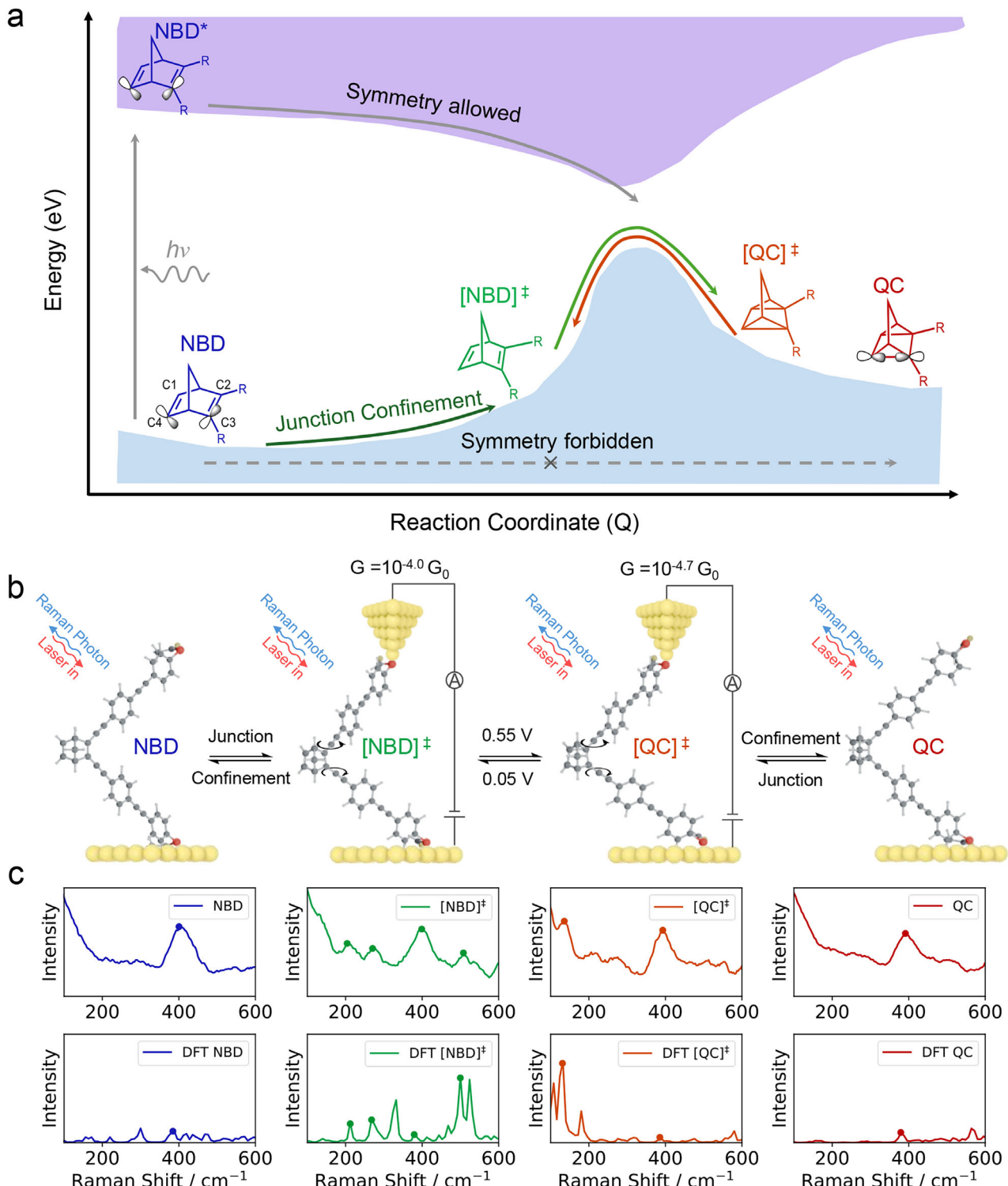


Figure 1. NBD-QC Reaction Pathways and Associated Raman Spectra. a) Schematic of reaction pathways for NBD to QC conversion. NBD (blue molecule) is typically converted to QC (red molecule) photochemically by exciting the NBD form (gray arrows) which relaxes to the QC form. Because of the orbital symmetry differences between the HOMO of NBD and QC there is a large barrier for the direct reaction between the two (dashed gray arrow). Alternatively, the symmetry is modified through steric control in a nanoconfined single-molecule junction (solid green arrow), thus enabling the reaction to be electrically driven at modest bias voltages. b) Schematic of the reaction pathway explored in this work. Using electrodes to modify the molecular configuration of the molecule to a point near the transition point decreases the resulting energy barrier enabling electrical control over the reaction. c) Examples of Raman spectra obtained for the system in each of the configurations explored. The upper panel shows experimental spectra, and lower panel are spectra calculated using DFT. Differences in the Raman spectra at each of the points enable tracking of the molecular configuration and identification of the emergence of configurations near the transition point.

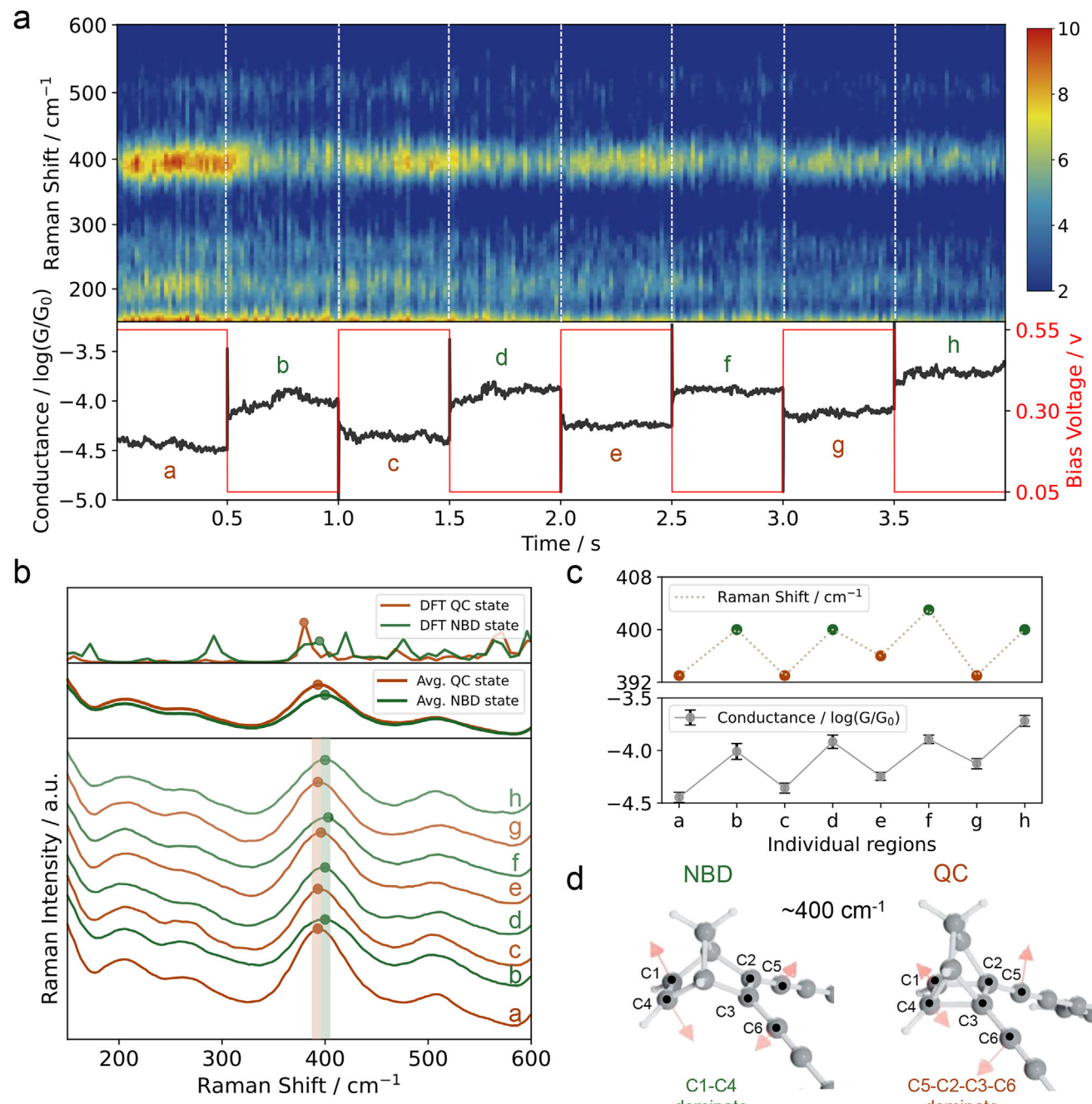


Figure 2. Simultaneous Single-Molecule Raman and Conductance Studies of Electrically Catalyzed NBD-QC Reactions. a) Simultaneous Raman spectroscopy (upper panel) and conductance (black) obtained while a square wave modulated bias voltage (red) is applied to the molecular junction. The dotted white lines split the Raman spectra into different regions depending on the applied bias voltage. A common minimum value is subtracted from all Raman spectra for clarity. b) Lower panel shows the averaged Raman spectrum obtained at each bias voltage for each of the regions in a. Middle panel displays the averaged Raman spectra obtained in the NBD (green) and QC (orange) states at bias voltage equal to 0.05 and 0.55 V respectively. Upper panel plots the DFT-calculated Raman spectra of the NBD and QC states. c) Lower panel shows averaged conductance for each of the time intervals identified in a, and upper panels plot the Raman shift of NBD (green) and QC (orange) states from the peak fitting of Figure 3b between 340 and 440 cm^{-1} respectively. All Raman spectra are filtered using a Savitzky Golay filter (see Figure S5, Supporting Information). d) Represent vibrational mode of NBD and QC $\approx 400 \text{ cm}^{-1}$.

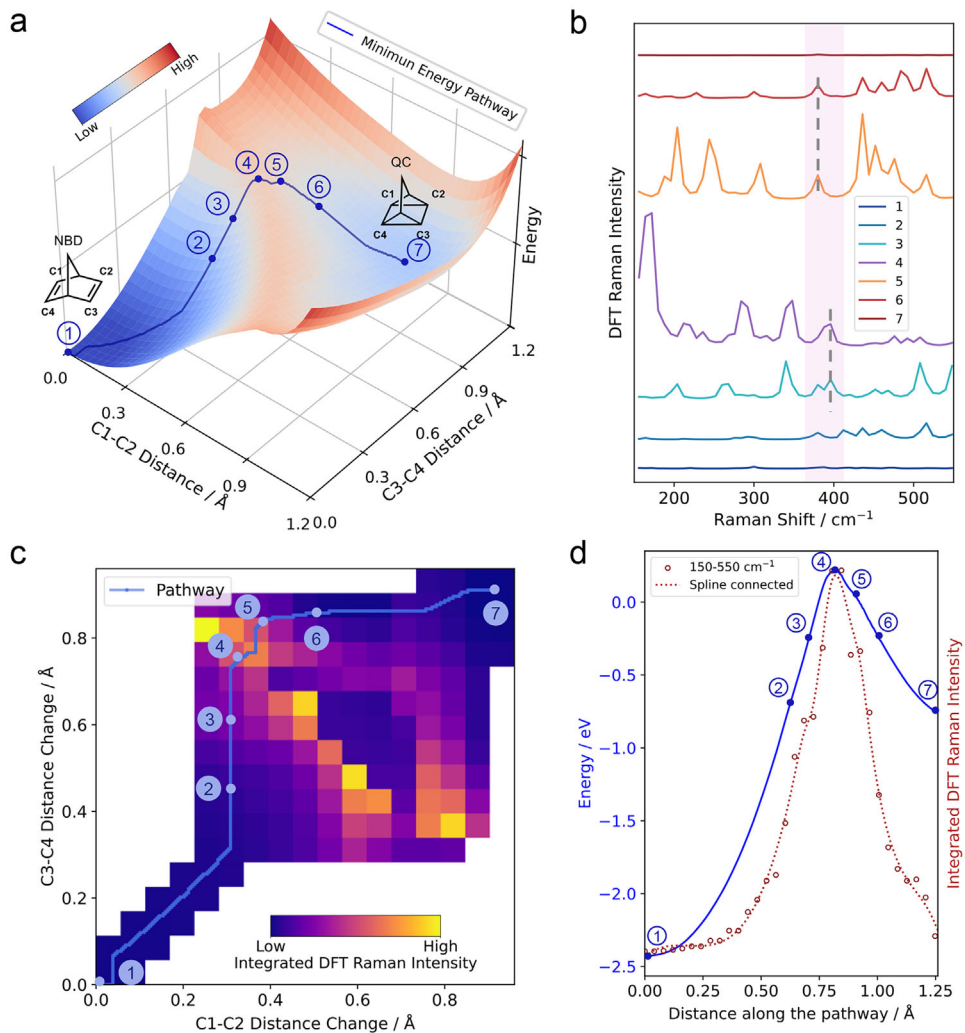


Figure 3. DFT Calculation of NBD to QC Reaction. a) Energy surface plot under steric control and electrical field of the reaction between NBD and QC state. The blue line shows minimum energy pathway. Blue dots indicate the seven representative states during the reaction. b) Individual Raman spectra along the minimum reaction pathway labeled in a, c and d. The dotted lines demonstrate the trend of $\approx 400 \text{ cm}^{-1}$ Raman peaks change from $[\text{NBD}]^{\ddagger}$ to $[\text{QC}]^{\ddagger}$. c) Integration of the 2D Raman spectrum from 150 to 550 cm^{-1} throughout the energy landscape. As with a, the blue curve corresponds to the minimum energy path. d) Energy (blue) and its corresponding Raman intensity integral along the minimum reaction pathway. The red dots correspond to 33 different molecular configurations along the minimum pathway, and the red curve is the connected spline of these points. The overlap of the two peaks of the Raman integral curve and the energy curve indicates that the Raman intensity increases as it exits the ground state and reaches its maximum near the transition point.

as the molecule switches between the NBD (high conductance) and QC (low conductance) forms. To compare the Raman shift of these two states more clearly, we average total Raman spectrum of QC and NBD state separately. As shown in the middle panel, the Raman shift of QC (393 cm^{-1}) is smaller than NBD (400 cm^{-1}). To examine the origins of this shift we perform Density Functional Theory (DFT) calculations of the two forms. Although the absolute shifts differ due to methodological and environmental factors,^[44,45] the experimental and theoretical trends are in good agreement, revealing that the QC peak has a red shift and intensity increase when compared to the NBD state (Figure 2b, upper panel). The calculation shows that the peaks observed in the experiment correspond to the vibrational modes of the molecular core unit (see Figure 2d). To demonstrate

this correlated change in molecular configuration, conductance, and spectra more clearly, we plot the averaged conductance and Raman shift of the $\approx 400 \text{ cm}^{-1}$ mode for each time region in Figure 2c. The conductance shows an alternating high and low values. Meanwhile, the alternating high and low Raman shift values between NBD state and QC state clearly provide a spectral fingerprint that verifies the electrically driven reaction between the two states.

Next, to examine the mechanism involved in this electrically-controlled reaction from the NBD to QC form, we calculate the potential energy landscape for a direct reaction between the two forms (Figure 3a). These calculations start from the minimized molecular configuration obtained when the molecule is attached to two gold electrodes and with an applied electric field across the

junction (see Experimental Section for details). The blue curve in Figure 3a,d shows that the calculated energy barrier for a thermally-activated transition from the NBD form to the QC form is extremely large (≈ 2.64 eV) as is expected from orbital symmetry conservation rules. Even with the applied bias (0.55 V), it is unlikely that the voltage alone will sufficiently increase the lattice temperature of the molecule to overcome such a large barrier.^[46,47] As such, there must be additional factors at play. It has previously been demonstrated that mechanical forces can be used to bypass orbital symmetry selection rules by biasing a reaction toward either a conrotatory or disrotatory pathway.^[10,11] Thus, we hypothesize that, in this case, steric confinement, induced by the two electrodes binding to the NBD-derivative, constrains the molecule into a configuration that is far from the ground state energy and is more favorable to the electrically induced reaction. To determine the feasibility of this hypothesis, we calculate the Raman spectra of the molecule throughout the potential energy landscape to identify Raman features that will enable us to test it directly. Figure 3b plots the spectra of seven such configurations along the lowest-barrier reaction pathway. From these calculations, a clear trend appears. In the energy minimized NBD and QC forms, points 1 and 7 respectively, there are practically no active Raman modes at low energies (between 150 and 550 cm⁻¹), but as one moves up the energy barrier nearer to the transition state, a range of modes starts appearing in this region, and the intensity of these modes increases substantially. In fact, as seen in Figure 3d, by examining Raman intensity between 150 and 550 cm⁻¹ of 33 spectra along this reaction pathway, we observe that this change in intensity directly tracks the change in the energy landscape, with a maximum intensity at the transition point energy. While specific vibrational modes may appear or disappear depending on the specific configuration, which may show difference to the observed spectra, the intensity of the Raman signal increases as the system moves closer to the transition point. Here we note that the ≈ 400 cm⁻¹ peak change is an exception (Figure 3b), as it exhibits robust and reproducible changes when the NBD-QC reaction occurs, due to the corresponding changes in the vibrational character from the altered bonding pattern at C2-C3 (single vs double bond in QC and NBD form respectively). This effect can be seen directly in Figure 3c where the Raman intensity is plotted throughout the potential energy landscape, where we find that the closer we are to the energy barrier, the greater the Raman intensity. This observation provides an unambiguous method of experimentally verifying the hypothesis. If the nanoconfinement from the electrodes is inducing a steric constraint that moves the molecule closer to the transition point, then the Raman spectra should display a significant increase in the visibility and intensity of modes in this low energy region in cases when the switching occurs.

To experimentally validate this hypothesis, we directly compare cases where switching occurs (Figure 4a,c,d) when the square-wave bias voltage is applied and those where it does not (Figure 4b,e,f). In the case of successful switching, both the conductance and the Raman shift ≈ 400 cm⁻¹ (Figure 4c) are observed, but in the case of failed switching both conductance and Raman shift (Figure 4e) remain unchanged, which provides a solid experimental basis for the successful modulation of this reaction and meanwhile rule out the possibility that the conductance and Raman changes originate from bias voltage induced

atomic motion in the electrodes.^[48–50] However, in addition to this 400 cm⁻¹ mode, in Figure 4a, several clear bands appear in the low energy region (150–550 cm⁻¹) as the system switches repeatedly from the NBD to QC form and back, as is predicted by the modeling done above. However, in Figure 4b only the ≈ 400 cm⁻¹ mode discussed above is readily visible. This observation is further confirmed by examining the average spectra from each of the conductance regions shown in Figure 4a,b, which are shown in Figure 4c,e, respectively. In the case of successful switching, obvious Raman modes appear at ≈ 200 , 270, and 515 cm⁻¹ for both the NBD (high conductance) and QC (low conductance) state regions, which all correspond to collective modes of the core unit which affect the C1-C2 and C3-C4 distance (see Figure S10, Supporting Information). Alternatively, in the cases where the switching is not observed, only rarely do any significant Raman features appear in this region, suggesting that the molecule is in a lower energy configuration on average in this junction.

To further confirm this observation, we examined 1915 Raman spectra from 30 switching events across 3 separate molecular junctions (half of the switches are from NBD to QC and half are QC to NBD) and 1001 spectra from 18 failed switching events across 3 different molecular junctions (see Supporting Information for details). In each case, we examined whether Raman peaks in the 150–550 cm⁻¹ region appeared in the spectrum (neglecting the ≈ 400 cm⁻¹ mode, which is nearly always present). In cases where the bias is switched from 0.05 to 0.55 V to induce the NBD to QC transition, these transition state modes appeared in 80.2% of the spectra when switching occurred, and for the 0.55 to 0.05 V transition (QC to NBD), these modes appeared in 76.1% of the spectra (Figure 4d). However, detectable peaks only appeared in 9.8% of the spectra in cases where the bias change failed to cause the molecular switch (Figure 4f).

These observations are consistent with the theoretical results shown in Figure 3. In particular, we note that traces 3, 4, and 5 in Figure 3b have intense modes ≈ 200 cm⁻¹, between 250 and 300 cm⁻¹, and above 500 cm⁻¹. While traces 2 and 6, which are only slightly above the ground state energies, display the 400 cm⁻¹ mode, but have very weak intensities across the rest of this region. Comparison with the results in Figure 4, this suggests that in cases where switching occurs the steric confinement from the nanogap forces into configurations that are far from the ground-state energy and near the transition state, thus enabling the transition. Here we note that the peak ≈ 400 cm⁻¹ represents the twisting mode of C1-C4/C5-C2-C3-C6 (see Figure 2d) in NBD/QC respectively, and the change in the active atoms correlates with the change of the single/double bond between C2-C3. The other peaks at 150 to 550 cm⁻¹ represent various scissoring modes of C1-C2/C3-C4 (see Figure S10, Supporting Information), they do not show a trend with C2-C3 bonding, but their appearance indicates that the molecule has moved up the energy barrier. We therefore conclude that this nanoconfined state has three important effects on the switching transition. First, as noted by previous studies of mechanochemical reactions, it biases the molecule toward a certain reaction pathway by sterically modifying the symmetry of the molecular orbitals.^[10,51,52] While the phase of the lobes may not be directly changed, the charge densities change, creating an asymmetry in the system, which

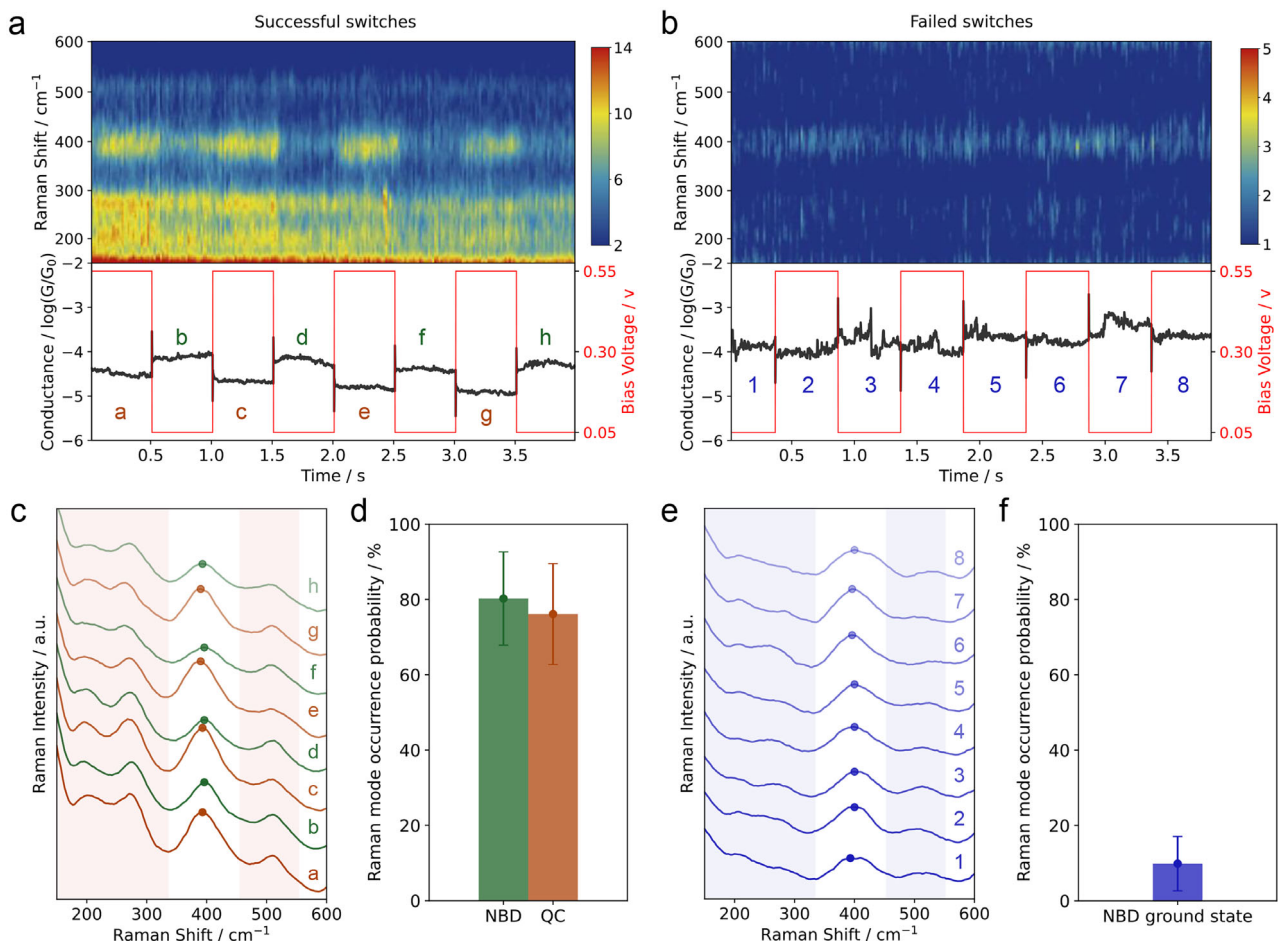


Figure 4. Analysis of Raman Spectra During Electrocatalyzed Reactions. **a,b)** Simultaneous Raman spectra and conductance changes with square wave bias voltage modulation of successful and failed switch events separately. **c)** Averaged Raman spectrum obtained at each bias voltage region of NBD (green) and QC (orange) from successful switching events (a). **d)** Raman mode occurrence probability of NBD and QC state, respectively, from 30 successful switching events. The spectral region that was used to calculate this probability is highlighted in (c) in red. **e)** Averaged Raman spectra obtained at each bias voltage region of the NBD ground state (blue) from failed switching events (b). **f)** Raman mode occurrence probability of the NBD ground state from 18 failed switch events. The Raman shift region that is used to calculate this probability is highlighted in (e) in blue.

softens the restrictions which in this case will favor a disconcerted reaction where a bond between one pair of carbon atoms will form first.^[53] Second, it increases the energy of the molecular system from its ground state, causing it to initially climb part of the way up the energy barrier, thus decreasing the total required energy needed to induce the reaction. As such, when a sufficient electrical voltage is applied, it can be driven over the barrier by activating molecular vibration modes, enabling an electrically-controlled, thermally-activated reaction from the NBD to QC form.^[38,54] And third, the nanoconfinement also stabilizes these high-energy configurations, which not only makes the reactions much more favorable in this direction,^[55] but enables the configurations near the transition state to be characterized *in situ* by Raman spectroscopy.

In conclusion, this work demonstrates that orbital symmetry selection rules can be relaxed in nanoconfined systems where high-energy configurations can be accessed and stabilized by forcing the molecular system into configurations that are

not thermally accessible at standard temperature and pressure. These results suggest that combining nanoconfinement with electrical control can yield new opportunities for developing low-energy catalytic pathways for high-energy-barrier reactions,^[56] and new prospects for characterizing transition states during these reactions.^[6] This biomimetic catalytic approach not only demonstrates the feasibility of inducing forbidden reactions but also opens new avenues for designing enzyme-inspired devices with broad implications for energy storage and molecular switching technologies.

2. Experimental Section

Sample Preparation: Gold substrates were prepared by evaporating $\approx 130 \text{ nm}$ gold onto the mica substrates and then cut into $\approx 1 \text{ cm} \times 2 \text{ cm}$ squares. Before using, the gold substrate is flame annealed with a butane torch for $\approx 10 \text{ s}$ to clean the surface. 0.1 mM L^{-1} NBD solution (DCM, Sigma-Aldrich) is dropped on the surface of the gold substrate to form

Self-assembled monolayer (SAM), which is rinsed by pure DCM and dried with N₂ stream before measurements.

Etched Tip Preparation: Obtaining ultra-sharp gold tips are a key factor for the enhancement of the Raman signal of molecular junction. Here we prepare the tip by using a modified electrochemical etching method that proposed by Ren et al.^[37] The electrolyte solution is combining pure ethanol (Sigma-Aldrich) with hydrochloric acid (Fisher Scientific, 37% weight concentration) as v: v = 1: 1. A gold ring that is made from gold wire (Sigma-Aldrich, 99.998%) is used as anode electrode and placed on the center surface of electrolyte solution. The same gold wire is cut to a length of 3 cm and submerged in the solution on the center of O ring to act as cathode. A constant \approx 2.6 V DC voltage is applied to the electrodes and the real-time current monitored. After its current drops to \approx 0 A, the tip is rinsed with deionized water and dried with a gentle N₂ stream.

SMBJ Combined Raman Spectroscopy: Our simultaneous conductance and Raman measurement system is composed of a lab-developed lateral SMBJ and a commercial Raman microscope (WITec Alpha 300R). The laser is first generated from a 785 nm diode laser (Toptica, XTRA II) and then focused on the molecular junction through a 100 \times objective lens (0.75 NA and 4.1 mm working distance). The laser light is linearly polarized and aligned to parallel to the tip axis in the SMBJ system. The scattered light is collected by CCD, with 8.8 ms resolution. This system is controlled by a LabVIEW program and the spectral data is collected in concert with the current which flow through the junction simultaneously. All Raman measurements are carried out by setting the laser power in range between 3 and 5 mW. The break junction system includes an optical stage (Thorlabs, LNR25D). A stepper motor is used to drive the coarse movement of substrate and then the gap distance. A tip holder is fixed on a ceramic piezo-electric block (Thorlabs, PC4FL, 4.6 μ m max displacement at its maximum voltage 150 V), which holds the gold tip and controls the fine movement. A commercial data acquisition card (NI PCIe-6353, 16-bit, \pm 10 V) is used to collect experimental data and a custom LabVIEW program was used to simultaneously control and measure the Raman and conductance signal.

DFT Calculations: The potential energy landscape and minimum energy path are calculated using flexural scans of the C1–C2 and C3–C4 bond lengths with a step size of 0.06 Å. The calculation used the B3LYP/LANL2DZ functional and basis in Gaussian 16. The initial configurations of the molecules used in the flexural scans are derived from optimized molecular junctions connected to gold electrodes. The dihedral angle of the C5–C2–C3–C6 was kept constant during the flexural scan to mimic the restriction of molecular degrees of freedom imposed by the presence of the gold electrodes. The energy plot has a total of 441 points, and Figure 3a shows the 250 \times 250 matrix formed by interpolating these points using the “cubic” method. B3LYP/LANL2DZ is also used for the Raman spectra calculations. Figure 3c was obtained by calculating the integral of the Raman spectra integral for each of the molecular structure during the reaction. In calculating the Raman intensity integrals along the minimum energy path, the average value of the Raman integrals of the points covered by a range of 0.12 Å radius centered on the point on the path was used. Computational corrections to the energy values were obtained using the DEF2TZVP basis set.

Supporting Information

Supporting Information is available from the Wiley Online Library or from the author.

Acknowledgements

This work was supported by the U.S. National Science Foundation. (NSF-2239226 and NSF-2328217) as well as the Keck Foundation. Support from the European Innovation Council (EIC) under the project ESiM (grant agreement No 101046364)

Conflict of Interest

The authors declare no conflict of interest.

Author Contributions

J.H. and R.L. originally conceived the idea and designed the experiments. R.L. and D.Z. performed the experiments and analysed the data. R.L. and F.S. performed the theoretical calculations. S.G., P.F., and K.M. synthesized the target molecule. All authors contributed to the manuscript.

Data Availability Statement

The data that support the findings of this study are available from the corresponding author upon reasonable request.

Keywords

forbidden reaction, nanoconfinement effect, Raman spectroscopy, reversible reaction, single-molecule device

Received: June 20, 2025
Revised: October 17, 2025
Published online:

- [1] B. Dong, Y. Pei, F. Zhao, T. W. Goh, Z. Qi, C. Xiao, K. Chen, W. Huang, N. Fang, *Nat. Catal.* **2018**, *1*, 135.
- [2] G. E. Lienhard, *Science* **1973**, *180*, 149.
- [3] A. Warshel, P. K. Sharma, M. Kato, Y. Xiang, H. Liu, M. H. M. Olsson, *Chem. Rev.* **2006**, *106*, 3210.
- [4] R. Breslow, *Science* **1982**, *218*, 532.
- [5] A. C. Aragones, N. L. Haworth, N. Darwish, S. Ciampi, N. J. Bloomfield, G. G. Wallace, I. Diez-Perez, M. L. Coote, *Nature* **2016**, *531*, 88.
- [6] H. Chen, C. Jia, X. Zhu, C. Yang, X. Guo, J. F. Stoddart, *Nat. Rev. Mater.* **2022**, *8*, 165.
- [7] J. Orrego-Hernández, A. Dreos, K. Moth-Poulsen, *Acc. Chem. Res.* **2020**, *53*, 1478.
- [8] R. B. Woodward, R. Hoffmann, *J. Am. Chem. Soc.* **1965**, *87*, 395.
- [9] R. B. Woodward, R. Hoffmann, *Angew. Chem., Int. Ed.* **1969**, *8*, 781.
- [10] C. R. Hickenboth, J. S. Moore, S. R. White, N. R. Sottos, J. Baudry, S. R. Wilson, *Nature* **2007**, *446*, 423.
- [11] J. Wang, T. B. Kouznetsova, Z. Niu, M. T. Ong, H. M. Klukovich, A. L. Rheingold, T. J. Martinez, S. L. Craig, *Nat. Chem.* **2015**, *7*, 323.
- [12] S. Ciampi, N. Darwish, H. M. Aitken, I. Diez-Perez, M. L. Coote, *Chem. Soc. Rev.* **2018**, *47*, 5146.
- [13] O. Bunjes, D. Hedman, A. Rittmeier, L. A. Paul, I. Siewert, F. Ding, M. Wenderoth, *Sci. Adv.* **2022**, *8*, abq7776.
- [14] X. Huang, C. Tang, J. Li, L. C. Chen, J. Zheng, P. Zhang, J. Le, R. Li, X. Li, J. Liu, Y. Yang, J. Shi, Z. Chen, M. Bai, H. L. Zhang, H. Xia, J. Cheng, Z. Q. Tian, W. Hong, *Sci. Adv.* **2019**, *5*, aaw3072.
- [15] S. Sevim, R. Sanchis-Gual, C. Franco, A. C. Aragonès, N. Darwish, D. Kim, R. A. Picca, B. J. Nelson, E. Ruiz, S. Pané, I. Diez-Pérez, J. Puigmartí-Luis, *Nat. Commun.* **2024**, *15*, 790.
- [16] A. Nitzan, M. A. Ratner, *Science* **2003**, *300*, 1384.
- [17] M. Taniguchi, M. Tsutsui, K. Shoji, H. Fujiwara, T. Kawai, *J. Am. Chem. Soc.* **2009**, *131*, 14146.
- [18] J. M. Beebe, B. Kim, J. W. Gadzuk, C. Daniel Frisbie, J. G. Kushmerick, *Phys. Rev. Lett.* **2006**, *97*, 026801.
- [19] K. D. Borne, J. C. Cooper, M. N. R. Ashfold, J. Bachmann, S. Bhattacharyya, R. Boll, M. Bonanomi, M. Bosch, C. Callegari, M. Centurion, M. Coreno, B. F. E. Curchod, M. B. Danailov, A. Demidovich, M. Di Fraia, B. Erk, D. Facciola, R. Feifel, R. J. G. Forbes, C. S. Hansen, D. M. P. Holland, R. A. Ingle, R. Lindh, L. Ma, H. G. McGhee, S. B. Muvva, J. P. F. Nunes, A. Odate, S. Pathak, O. Plekan, et al., *Nat. Chem.* **2024**, *16*, 499.

- [20] J. Mony, C. Climent, A. U. Petersen, K. Moth-Poulsen, J. Feist, K. Börjesson, *Adv. Funct. Mater.* **2021**, *31*, 2010737.
- [21] T. Brunck, F. Weinhold, *J. Am. Chem. Soc.* **1979**, *101*, 1700.
- [22] C. Qin, Z. Zhao, S. R. Davis, *J. Mol. Struct. Theochem* **2005**, *728*, 67.
- [23] T. Deckert-Gaudig, A. Taguchi, S. Kawata, V. Deckert, *Chem. Soc. Rev.* **2017**, *46*, 4077.
- [24] S. Lukin, K. Užarević, I. Halasz, *Nat. Protoc.* **2021**, *16*, 3492.
- [25] P. Verma, *Chem. Rev.* **2017**, *117*, 6447.
- [26] R. Zhang, Y. Zhang, Z. C. Dong, S. Jiang, C. Zhang, L. G. Chen, L. Zhang, Y. Liao, J. Aizpurua, Y. Luo, J. L. Yang, J. G. Hou, *Nature* **2013**, *498*, 82.
- [27] C. V. Raman, K. S. Krishnan, *Nature* **1928**, *121*, 501.
- [28] E. M. Dief, P. J. Low, I. Díez-Pérez, N. Darwish, *Nat. Chem.* **2023**, *15*, 600.
- [29] L. Rincón-García, A. K. Ismael, C. Evangelista, I. Grace, G. Rubio-Bollinger, K. Porfyrikis, N. Agraït, C. J. Lambert, *Nat. Mater.* **2016**, *15*, 289.
- [30] D. Xiang, H. Jeong, T. Lee, D. Mayer, *Adv. Mater.* **2013**, *25*, 4845.
- [31] Y. Kim, T. Pietsch, A. Erbe, W. Belzig, E. Scheer, *Nano Lett.* **2011**, *11*, 3734.
- [32] L. Domulevicz, H. Jeong, N. K. Paul, J. S. Gomez-Diaz, J. Hihath, *Angew. Chem., Int. Ed.* **2021**, *60*, 16436.
- [33] T. A. Su, H. Li, M. L. Steigerwald, L. Venkataraman, C. Nuckolls, *Nat. Chem.* **2015**, *7*, 215.
- [34] W. Haiss, C. Wang, I. Grace, A. S. Batsanov, D. J. Schiffrin, S. J. Higgins, M. R. Bryce, C. J. Lambert, R. J. Nichols, *Nat. Mater.* **2006**, *5*, 995.
- [35] T. Konishi, M. Kiguchi, M. Takase, F. Nagasawa, H. Nabika, K. Ikeda, K. Uosaki, K. Ueno, H. Misawa, K. Murakoshi, *J. Am. Chem. Soc.* **2013**, *135*, 1009.
- [36] C. Yang, Y. Li, S. Zhou, Y. Guo, C. Jia, Z. Liu, K. N. Houk, Y. Dubi, X. Guo, *Nat. Chem.* **2023**, *15*, 972.
- [37] R. Chikkaraddy, B. de Nijs, F. Benz, S. J. Barrow, O. A. Scherman, E. Rosta, A. Demetriadou, P. Fox, O. Hess, J. J. Baumberg, *Nature* **2016**, *535*, 127.
- [38] H. B. Li, B. E. Tebikachew, C. Wiberg, K. Moth-Poulsen, J. Hihath, *Angew. Chem., Int. Ed.* **2020**, *59*, 11641.
- [39] B. E. Tebikachew, H. B. Li, A. Pirrotta, K. Börjesson, G. C. Solomon, J. Hihath, K. Moth-Poulsen, *J. Phys. Chem. C* **2017**, *121*, 7094.
- [40] D. P. dos Santos, M. L. A. Temperini, A. G. Brolo, *Acc. Chem. Res.* **2019**, *52*, 456.
- [41] D. R. Ward, N. J. Halas, J. W. Ciszek, J. M. Tour, Y. Wu, P. Nordlander, D. Natelson, *Nano Lett.* **2008**, *8*, 919.
- [42] J. R. Lombardi, R. L. Birke, G. Haran, *J. Phys. Chem. C* **2011**, *115*, 4540.
- [43] L. Domulevicz, H. Jeong, N. K. Paul, J. S. Gomez-Diaz, J. Hihath, *Angew. Chem., Int. Ed.* **2021**, *60*, 16436.
- [44] A. P. Scott, L. Radom, *J. Phys. Chem.* **1996**, *100*, 16502.
- [45] B. Pettinger, B. Ren, G. Picardi, R. Schuster, G. Ertl, *Phys. Rev. Lett.* **2004**, *92*, 096101.
- [46] D. G. de Oteyza, P. Gorman, Y.-C. Chen, S. Wickenburg, A. Riss, D. J. Mowbray, G. Etkin, Z. Pedramrazi, H.-Z. Tsai, A. Rubio, *Science* **2013**, *340*, 1434.
- [47] W. Ho, *J. Chem. Phys.* **2002**, *117*, 11033.
- [48] S. Liu, F. P. Bonafe, H. Appel, A. Rubio, M. Wolf, T. Kumagai, *ACS Nano* **2023**, *17*, 10172.
- [49] B. Cirera, S. Liu, Y. Park, I. Hamada, M. Wolf, A. Shiotari, T. Kumagai, *Phys. Chem. Chem. Phys.* **2024**, *26*, 21325.
- [50] S. Kaneko, D. Murai, S. Marqués-González, H. Nakamura, Y. Komoto, S. Fujii, T. Nishino, K. Ikeda, K. Tsukagoshi, M. Kiguchi, *J. Am. Chem. Soc.* **2016**, *138*, 1294.
- [51] M. K. Beyer, H. Clausen-Schaumann, *Chem. Rev.* **2005**, *105*, 2921.
- [52] Q.-Z. Yang, Z. Huang, T. J. Kucharski, D. Khvostichenko, J. Chen, R. Boulatov, *Nat. Nanotechnol.* **2009**, *4*, 302.
- [53] K. Jorner, A. Dreos, R. Emanuelsson, O. El Bakouri, I. F. Galván, K. Börjesson, F. Feixas, R. Lindh, B. Zietz, K. Moth-Poulsen, H. Ottosson, *J. Mater. Chem. A* **2017**, *5*, 12369.
- [54] B. C. Stipe, M. A. Rezaei, W. Ho, S. Gao, M. Persson, B. I. Lundqvist, *Phys. Rev. Lett.* **1997**, *78*, 4410.
- [55] D. Stefani, K. J. Weiland, M. Skripnik, C. Hsu, M. L. Perrin, M. Mayor, F. Pauly, H. S. J. van der Zant, *Nano Lett.* **2018**, *18*, 5981.
- [56] J. I. Seeman, *J. Org. Chem.* **2015**, *80*, 11632.
- [57] B. Ren, G. Picardi, B. Pettinger, *Rev. Sci. Instrum.* **2004**, *75*, 837.